mathematics

MDPI

Article

Research and Implementation of Denoising Algorithm for Brain MRIs via Morphological Component Analysis and Adaptive Threshold Estimation

Buhailiqiemu Awudong [1,2], Paerhati Yakupu [1], Jingwen Yan [3,4] and Qi Li [1,2,*]

[1] School of Computer Science and Technology, Changchun University of Science and Technology, 7089 Weixing Road, Changchun 130022, China; 2018200094@mails.cust.edu.cn (B.A.); py@mails.cust.edu.cn (P.Y.)
[2] Zhongshan Institute of Changchun University of Science and Technology, 16 Huizhan East Road, Zhongshan 528437, China
[3] Department of Electronic Engineering, Shantou University, 243 Daxue Road, Shantou 515063, China; jwyan@stu.edu.cn
[4] Key Laboratory of Intelligent Manufacturing Technology, Ministry of Education, Shantou University, 243 Daxue Road, Shantou 515063, China
* Correspondence: liqi@cust.edu.cn; Tel.: +86-431-85583546

Abstract: The inevitable noise generated in the acquisition and transmission process of MRIs seriously affects the reliability and accuracy of medical research and diagnosis. The denoising effect for Rician noise, whose distribution is related to MR image signal, is not good enough. Furthermore, the brain has a complex texture structure and a small density difference between different parts, which leads to higher quality requirements for brain MR images. To upgrade the reliability and accuracy of brain MRIs application and analysis, we designed a new and dedicated denoising algorithm (named VST–MCAATE), based on their inherent characteristics. Comparative experiments were performed on the same simulated and real brain MR datasets. The peak signal-to-noise ratio (PSNR), and mean structural similarity index measure (MSSIM) were used as objective image quality evaluation. The one-way ANOVA was used to compare the effects of denoising between different approaches. $p < 0.01$ was considered statistically significant. The experimental results show that the PSNR and MSSIM values of VST–MCAATE are significantly higher than state-of-the-art methods ($p < 0.01$), and also that residual images have no anatomical structure. The proposed denoising method has advantages in improving the quality of brain MRIs, while effectively removing the noise with a wide range of unknown noise levels without damaging texture details, and has potential clinical promise.

Keywords: MRIs denoising; variance-stabilizing transformation (VST); morphological component analysis (MCA); sparse representation; local adaptive thresholds

MSC: 94A08

check for updates

Citation: Awudong, B.; Yakupu, P.; Yan, J.; Li, Q. Research and Implementation of Denoising Algorithm for Brain MRIs via Morphological Component Analysis and Adaptive Threshold Estimation. *Mathematics* **2024**, *12*, 748. https://doi.org/10.3390/math12050748

Academic Editors: Joanna Czajkowska, Jan Juszczyk and Joanna Jaworek-Korjakowska

Received: 13 January 2024
Revised: 17 February 2024
Accepted: 27 February 2024
Published: 1 March 2024

Copyright: © 2024 by the authors. Licensee MDPI, Basel, Switzerland. This article is an open access article distributed under the terms and conditions of the Creative Commons Attribution (CC BY) license (https://creativecommons.org/licenses/by/4.0/).

1. Introduction

Magnetic resonance (MR) imaging is a kind of tomography technology, which reconstructs the human body's information by processing the captured MR signals [1]. In the acquisition process, due to the limitation of hardware circuit and the object to be imaged, as well as the influence of sensors and interference of transmission channel in the transmission process, magnetic resonance images (MRIs) will be polluted and noise points will be generated in the image, which affects the reliability and accuracy of clinical diagnosis and medical research. Therefore, before further analysis and processing of MRIs, it is necessary to preprocess the image to reduce the impact of noise [2].

At present, researchers have investigated many kinds of digital image denoising methods, but generally for ordinary images or directly for medical MRIs using ordinary

image denoising algorithms. The most commonly used noise model in common images is the additive noise model, in which the noise is independent of original image signal, and has a Gaussian distribution of zero-mean and known standard deviation. Previous studies have shown that the noise of MRIs mainly obeys the Rician distribution [3–5], hence the noise in MRIs no longer belongs to additive noise, and the noise intensity is related to the original image signal. Some denoising algorithms suitable for ordinary images are not suitable for MRI denoising.

As shown in Figure 1, (a) is the noise-free T1w MRI obtained from IXI Dataset 2021 [6], and (b) to (e) are noisy images obtained by adding noise to (a). The types of noise are the Gaussian noise with mean value 0 and variance 10, the Rician noise with noise intensity of 10%, the Salt and Pepper noise with noise density of 10%, and the Rayleigh noise. It can be seen that, after adding different types of noise, the images are different from each other, which means the mathematical principle of the denoising algorithm is also different.

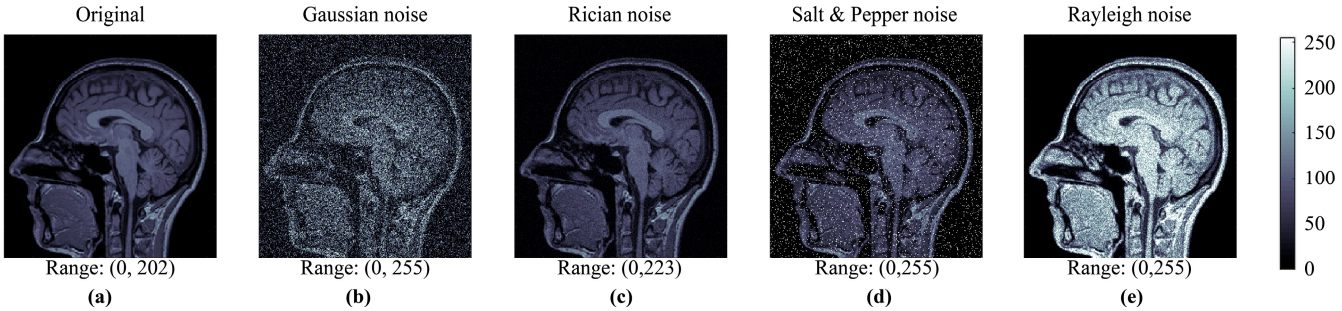

Figure 1. Noise-free brain MRI (from normal, healthy subjects, IXI002-Guys-0828-T1 in IXI Dataset 2021) and its four types of noise contaminated images. (**a**) is the noise-free T1w MRI, and (**b**–**e**) are noisy images obtained by adding noise to (**a**). The types of noise are the Gaussian noise with mean value 0 and variance 10, the Rician noise with noise intensity of 10%, the Salt and Pepper noise with noise density of 10%, and the Rayleigh noise.

The main task of image denoising is to use various filtering techniques to filter out noise while protecting important information such as image details [7–9]. Filtering can be carried out in time domain, such as Gaussian filter [10], Wiener filter [11], bilateral filter [12], total variation (TV) filter [13], and nonlocal mean (NLM) filter [14]; it can also be used in the transform domain, such as wavelet threshold filtering [15], and curvelet threshold filtering [16,17], etc. However, the above filtering methods are all designed to remove noise obeying Gaussian distribution. If they are directly applied to Rician noise removal, the performance cannot get the expected results. At present, some good medical image denoising algorithms, such as deep evolutionary networks with an expedited genetic algorithm [18]; NeighShrink, which is based on chi-square unbiased risk estimation [19]; biquadratic polynomial, with minimum error constraints and low-rank approximation [20]; and weighted nuclear norm minimization (WNNM) [21], etc., have obtained good MRI denoising effect. However, these methods did not consider that the characteristics of the Rician noise distribution of MRIs are relevant to image data, and that its variance changes with the change of the data. To better illustrate these problems, we show the example of the noise reduction results of the WNNM method in Figure 2. Figure 2e contains a lot of texture information about brain MRIs, which means the WNNM method does not do well in protecting the brain texture structure in detail in the process of denoising. Deep learning-based image denoising methods have also been investigated recently; however, although they achieved impressive results [22,23], they have a high computational cost and require a huge training data set. The noise reduction performance of deep learning depends on the training data, but the reference image data that can be obtained from the simulated dataset is not sufficient.

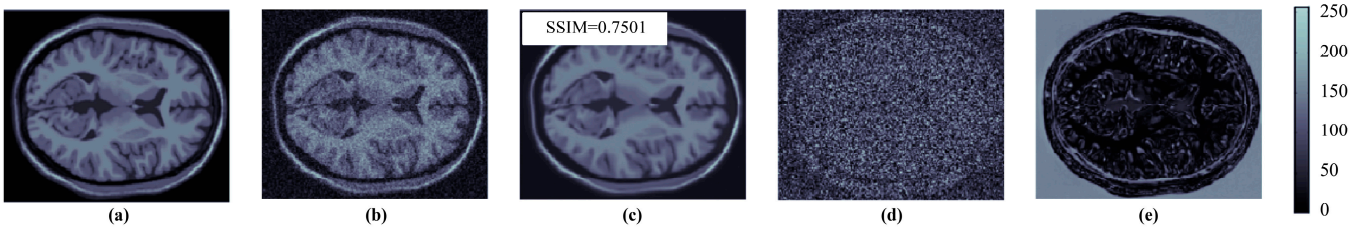

Figure 2. (**a**) Noise-free image; (**b**) Noisy MRI distributed by Rician noise; (**c**) Denoised MRI by WNNM; (**d**) Residual image (absolute difference between (**b**,**c**)); (**e**) The lost structure components (absolute difference between (**a**,**c**)).

One of the methods to remove the Rician noise is to remove the Gaussian noise in the real part and imaginary part signals, respectively, and then reconstruct the MRI; however, it is easy to cause the reconstructed image to be accompanied by "ringing artifacts" because of the phase error. In order to solve the application problem of filtering technology in Rician distribution noise, Nowak [24] proposed a method to reduce the correlation between image data and noise by modulus square of MRI, and then used the filtering method to denoise the modulus square image with deviation correction; subsequently, FOI A. [25] proposed the framework of variance-stabilizing transformation (VST). The methods of modulus square and VST provide a new way for Rician noise removal, and have therefore been widely used in MRI denoising in recent years [26,27]. While these methods improve the effectiveness of removing Rician noise, problems of threshold selection and lack of edge protection still remain.

In the noisy image, the frequency of useful information is low, whereas the frequency of noise is high. On the one hand, the image edge, texture, and other details are predominantly scattered in the high frequency part, whereas the flat region information is mainly distributed in the low frequency part. On the other hand, although image noise is mainly a high frequency component, it also comprises low frequency components, which results in the overlapping of useful information and noise in the frequency band. Morphological component analysis [28] (MCA) has potential advantages in image super-resolution applications, due to its ability to combine sparse representation theory and variational method to decompose images.

The brain has a complex texture structure and a small density difference between different parts, which leads to higher quality requirements for brain MRIs, and makes MR denoising much more challenging. The main purpose of this study is to repair the tampered pixel values of brain MRIs during the acquisition and transmission operation, and provide clearer and more reliable noiseless images. In order to avoid the "ringing artifacts" accompanied with denoised MRIs, we decided against denoising the original real part signals and imaginary part signals, respectively, and instead applied VST to MRIs reconstructed from real part signals and imaginary part signals, and set adaptive thresholds for texture and smooth regions decomposed by MCA. In order to remove the noise as much as possible without misclassifying the non-noisy pixel, we considered both the variance of the noisy pixel and the variance of the non-noisy pixel when setting the local adaptive thresholds.

2. Materials and Methods

In this experiment, we used real clinical MR data from brain tumor patients. Before doing the experiment, all datasets were reviewed by the appropriate ethics committee. Since all datasets used in our study are public datasets, which do not pose any potential risks to individuals or individual privacy and can be publicly accessed online without restrictions, the ethics committee indicated that ethical approval was not required.

The imaging principle of MRIs is different from that of other types of images, which leads to differences in the noise they contain. In order to better describe and analyze the characteristics and distribution of noise in MRIs to develop a more suitable and dedicated

denoising algorithm for MRIs, we first set a model for noise according to the principle of MRIs formation. On this basis, we propose a novel denoising algorithm (named VST–MCAATE). In applying VST–MCAATE, we sought to accurately estimate noise levels and simplify parameter selection by eliminating the correlation between noise and MRI signal; we then fixed the noise variance in the MRI by using variance-stabilizing transformation (VST); in then seeking to resolve the problem of the overlapping of useful information and noise in the frequency band (which can in turn can preserve complex texture details of MRIs while denoising), we used morphological component analysis (MCA). During this process, we also improved the MCA to solve the problem of unfavourable signal processing and storage due to information redundancy—in order to ensure the model has a better ability to identify noisy and non-noisy pixels, the variance of the noisy pixel and the variance of the non-noisy pixel both were both taken into consideration when setting the threshold model; furthermore, we also set the threshold to locally adaptive in order to avoid a fuzzy effect and keep detailed information. In this chapter, we will provide a detailed explanation of the dataset, noise model, MCA (and its improvements), dictionary selection, overall denoising model framework, denoising performance evaluation criteria, and denoising significance analysis methods.

2.1. Datasets

Real clinical MRIs cannot be obtained without any noise. Therefore, in order to use noise-free images as numerical references for objective evaluation indicators, we use the simulated brain database (SBD) [29] which is taken from the brain-imaging center at Montreal Institute of Neurology, McGill University. This simulated database consists of two anatomical models, such as normal brain MR data and MS (multiple sclerosis) lesion brain data, and provides brain MRIs in T1w, T2w, and PDw modalities. Since MR data from different modalities have different properties, which lead to differences between images in different modalities, this paper performs noise reduction tests on MR data from each of the three modalities separately. We set slice thickness = 1 mm, Intensity non-uniformity = 0%. Add Rician noise with the single intensity of 3%, 5%, 7%, and 9% to imitate the noised MRIs. Our experimental data then consisted of three modalities, five noise level types, and two anatomical models. In addition to using synthetic datasets, we also used two real clinical brain MRI datasets [6,30] to further illustrate the advantages of this method. (1) The Whole Brain Atlas dataset: 113 T1w, 184 T2w, 136 PDw neoplastic disease (brain tumor) MRIs from Harvard Medical School. (2) IXI Dataset (2021): 581 T1w, 578 T2w, 578 PDw 3-dimensional normal, healthy brain MRIs from Imperial College London.

2.2. Noise Model for MRIs

The causes of noise determine the characteristics of noise distribution, and its relationship with image signals. MRI's original signal comes from the real part and the imaginary part of the receiving coil of the equipment, and the signal from each of these two channels has the additive Gaussian white noise with a mean value of 0. MRI data are obtained by sampling signals from two channels and conducting Fourier transform reconstruction. Due to the linearity and orthogonality of the Fourier transform, the reconstructed MRI data still contains complex Gaussian white noise. For image subsequent processing and visual requirements, take modulo calculation of the reconstructed data of real and imaginary parts, and let the length of the corresponding vector on the complex plane represent the pixel values to obtain the final visual MRI image. The modulo calculation transforms the noise distribution of MRI from a complex Gaussian distribution to a Rician distribution, which is the cause of the Rician distribution noise in the MRI.

The reconstructed data of MRIs can be expressed as:

$$X = X_{real} + iX_{imaginary} = (F\cos\theta + \xi_1) + i(F\sin\theta + \xi_2), \quad (1)$$

where X_{real} and $X_{imaginary}$ are real and imaginary signals, respectively, F and θ are the amplitude and phase of the image's original signal, and ξ_1 and ξ_2 are independent additive Gaussian white noise with mean 0 and variance σ^2.

Visual MRIs are obtained by modulo calculation of reconstructed data,

$$G = |X| = \sqrt{(F\cos\theta + \xi_1)^2 + (F\sin\theta + \xi_2)^2}. \quad (2)$$

The Formula (2) indicates that the noise in the Visual MRI G is no longer additive Gaussian white noise independent of the image data, and its Gaussian distribution changes to Rician distribution related to the original image data. The probability density function is,

$$P(G|F,\sigma) = \frac{G}{\sigma^2}\exp\left(\frac{-(G^2+F^2)}{2\sigma^2}\right)I_0\left(\frac{G\times F}{\sigma^2}\right), \quad (3)$$

$$I_n(x) = \sum_{m=0}^{\infty}\frac{(-1)^m(x/2)^{n+2m}}{m!\Gamma(n+m+1)}, \quad (4)$$

where G is the noisy MRI, F is the original noise-free image, σ is the standard deviation of Gaussian noise in the real and imaginary parts, and I_0 is the zero order first class Bessel functions, $I_n(x)$ is Bessel function [31].

When n is a positive integer or zero, $\Gamma(n+m+1)$=$(n+m)!$, therefore

$$I_0(x) = \sum_{m=0}^{\infty}\frac{(-1)^m(x/2)^{n+2m}}{m!(n+m)!} = \sum_{m=0}^{\infty}\frac{(-1)^m(x/2)^{2m}}{m!m!} = \sum_{m=0}^{\infty}\frac{1}{m!m!}\left(-\frac{x^2}{4}\right)^m. \quad (5)$$

When the signal-to-noise ratio (SNR) of MRIs is very low, the probability density function of MRI amplitude can be approximated as:

$$P(G|F,\sigma) \approx \frac{G}{\sigma^2}\exp\left(-G^2/2\sigma^2\right). \quad (6)$$

When the SNR of MRIs is high, the probability density function of MRI amplitude can be approximated as:

$$P(G|F,\sigma) \approx \frac{1}{\sqrt{2\pi}\sigma}\exp\left(-\left(G-\sqrt{F^2+\sigma^2}\right)^2/2\sigma^2\right). \quad (7)$$

It can be inferred from (6), (7), and Figure 3 that in the very low SNR area of MRI, the noise will degenerate to Rayleigh distribution from Rician distribution (with no signal, the distributions are exactly equivalent), whereas in the high SNR area it will degenerate to Gaussian distribution; at low-medium SNR, it is neither Gaussian nor Rayleigh. Therefore, the diversity and complex distribution of MRIs bring great difficulties to MRI denoising. When the SNR is high, some denoising methods aim at white Gaussian noise and, with an additional unbiased estimation strategy, can still be used for MRI denoising and achieve good results; however, for MRIs with low SNR, the noise reduction effect still needs to be improved. A feasible scheme is to use the maximum likelihood of Rician distribution to restore MRIs in the maximum posterior framework; however, the maximum posterior framework can only incorporate a limited prior, and its optimization process is relatively time-consuming. Another scheme is to transform the image amplitude to make the MRI's signal independent of the noise by VST—that is, to approximately transform Rician noise into additive Gaussian noise, and then adopt a noise reduction algorithm with excellent Gaussian noise removal effect to denoise, and finally obtain, an unbiased denoised image through inverse VST.

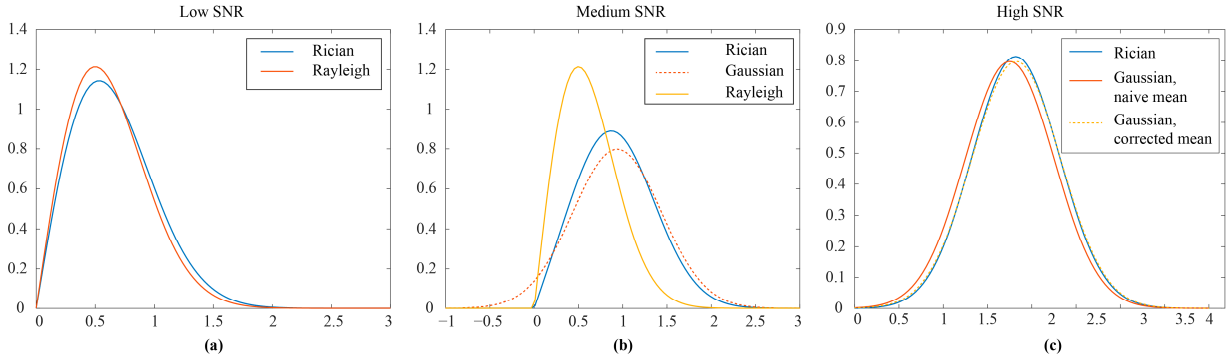

Figure 3. Probability density map at different SNR. (**a**) In the very low SNR area of MRI, the noise will degenerate to Rayleigh distribution from Rician distribution (with no signal, the distributions are exactly equivalent); (**b**) At low-medium SNR area, the noise is neither Gaussian nor Rayleigh; (**c**) In the high SNR area, the noise will degenerate to Gaussian distribution.

2.3. Variance-Stabilizing Transformation (VST)

The distribution of Rician noise is dependent on the image data, and its variance varies with the data. VST is used to transform the Rician noise in the MRI into a Gaussian distribution with stable variance, so that various filtering methods suitable for Gaussian noise can be used for denoising; the inverse VST transform is then performed to construct the denoised MRI [25].

The VST algorithm formula is

$$f(z) = \sqrt{z^2/\delta^2 - 0.5} + a, \tag{8}$$

where Z is the measurement signal, δ^2 is variance, a is a constant. In this paper, the measurement signal is noisy MRI images, and in (2)–(7) we use G to represent noisy MRI images, so

$$f(G) = \sqrt{G^2/\delta^2 - 0.5} + a. \tag{9}$$

$$a = f(G_{\max}) - \sqrt{G_{\max}^2/\delta^2 - 0.5}. \tag{10}$$

Let ϕ be the denoising method, and then denoise the image $f(z)$, with additive Gaussian noise after VST conversion to obtain image D, that is

$$D = \phi(f(G)). \tag{11}$$

The final denoising image I, can be obtained by the unbiased estimation of the inverse VST transform of D, as shown in the following formula:

$$I = f^{-1}(D) \approx \delta(D-a)^2/\sqrt{(D-a)^2 + 0.5}. \tag{12}$$

2.4. Morphological Component Analysis (MCA)

Starck et al. [28] assumed that for a given arbitrary signal S is linearly composed of K sub-elements with different shapes, that is, $S = \sum_{i=1}^{K} s_i$, where s_i represents the source signal or component of each different feature that composes the signal S. Let the dictionary accomplish sparseness within the class and different submodes between classes, so as to achieve the purpose of morphological component separation. The basic idea is to use the morphological differences of signal components to divide the image into texture and flat parts, which are applied to image decomposition and reconstruction, as shown in Figures 4 and 5 (for the convenience of description and comprehension, only the case of $i = 2$ is drawn in these figures, and a familiar, easy-to-understand diagram is used). $S_{Gaussians}$ and S_{Lines} respectively represent the smooth part and the texture part of the original image, and the superposition of the two can generate the original image;

noise may be introduced in the middle; $\Phi_{Gaussians}$ and Φ_{Lines} respectively represent the sparse dictionary of the smooth part and the texture part. The final framework of the MCA variational model proposed by Starck et al. [28] as:

$$\left\{\alpha_1^{opt}, \alpha_2^{opt}, \ldots, \alpha_i^{opt}\right\} = \arg\min_{\{\alpha_1,\alpha_2,\ldots,\alpha_i\}} \sum_{i=1}^{K} \|\alpha_i\|_1 + \lambda \left\| S - \sum_{i=1}^{K} \Phi_i \alpha_i \right\|_2^2, \tag{13}$$

$$\text{subject to}: \; S = \sum_{i=1}^{K} s_i = \sum_{i=1}^{k} \Phi_i \alpha_i, \tag{14}$$

where S is a linear combination of K sub-elements, s_i represents different types of sub-signals decomposed by S, α_i is the representation coefficient generated by the complete transformation of the signal s_i, L2 is the error norm, and Φ is for dictionary, which plays a key role in the MCA algorithm. The use of L2-norm for the residual in (13) is based on the assumption that the residual is a zero-mean Gaussian white noise distribution. There is a problem to consider: the solution obtained by (13) may be quite huge, because the dictionary is a collection of over-complete redundant bases, and the signal transformation based on the dictionary will naturally generate a large amount of redundant information (the capacity of α_i^{opt} is much larger than that of s_i). Although a large amount of redundant information can achieve the purpose of accurately representing the signal, it is not conducive to signal processing and storage. The problem of finding the representation vector $\{\alpha_1^{opt}, \alpha_2^{opt}, \cdots, \alpha_i^{opt}\}$ is transformed into finding K signal types $\{s_1, s_2, \cdots, s_i\}$; that is, finding K images can solve this problem. Therefore, the transform coefficient α_i^{opt} in (13) can be replaced by the source signal s_i that constitutes the signal S, namely:

$$\left\{s_1^{opt}, s_2^{opt}, \ldots, s_i^{opt}\right\} = \arg\min_{\{s_1,s_2,\ldots,s_i\}} \sum_{i=1}^{K} \|T_i s_i\|_1 + \lambda \left\| S - \sum_{i=1}^{K} s_i \right\|_2^2, \tag{15}$$

where T_i is the inverse transformation of the dictionary Φ_i. In this way, the unknown becomes an image instead of representing a coefficient. An important aspect of processing signals instead of coefficients is to add constraints to each individual signal s_i. Adding the constraint information for the source signal in (15), can obtain:

$$\left\{s_1^{opt}, s_2^{opt}, \ldots, s_i^{opt}\right\} = \arg\min_{\{s_1,s_2,\ldots,s_i\}} \sum_{i=1}^{K} \|T_i s_i\|_1 + \lambda \left\| S - \sum_{i=1}^{K} s_i \right\|_2^2 + \sum_{i=1}^{K} \gamma_i \xi_i(s_i). \tag{16}$$

Among them, $\xi_i(s_i)$ realizes the constraint on the component s_i. By solving (16), the components of the signal can be obtained.

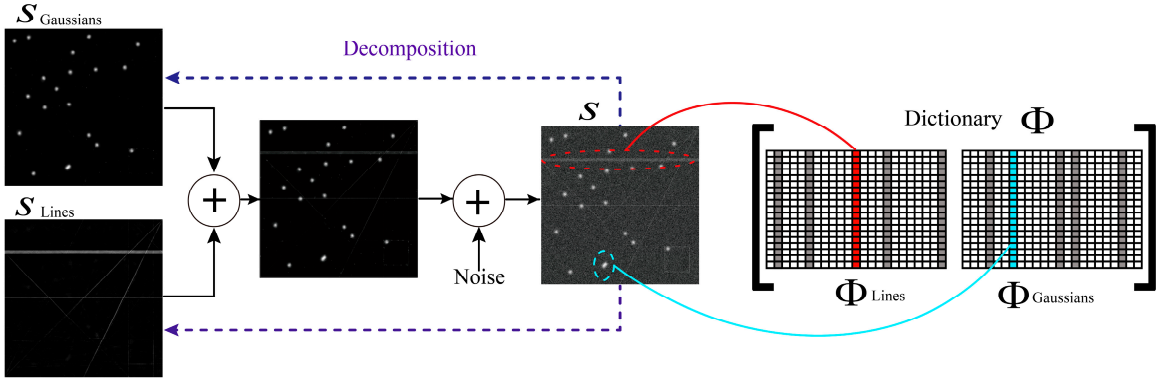

Figure 4. Schematic diagram of image decomposition and reconstruction using MCA algorithm (in the case where the input image only contains straight lines and isotropic Gaussian).

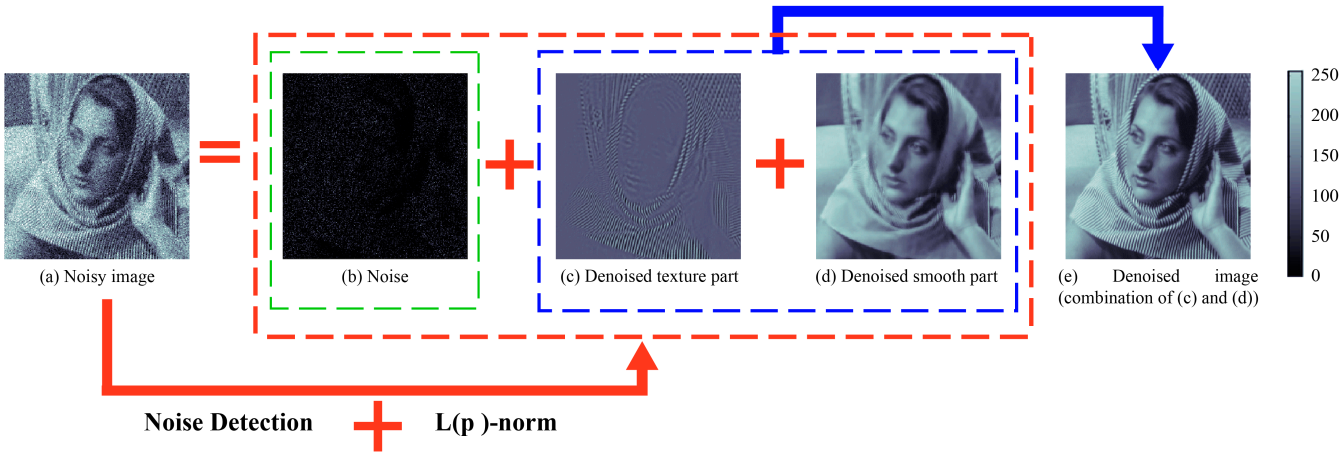

Figure 5. An instance of Barbara image decomposition and reconstruction using MCA algorithm.

2.5. Dictionary Selection

In image sparse decomposition, it is very crucial to design a suitable dictionary to approximate the sparse components. For expressing the smooth area, the most commonly used dictionaries are curvelet transform dictionary [32], local ridgelet transform dictionary [33,34], and porous algorithm dictionary; for texture regions, wavelet dictionary [35,36], Gabor dictionary [37], local discrete cosine transform dictionary [38], etc. In this article, we compared the advantages and disadvantages of these dictionaries, and considered their applicability to medical images before choosing the curvelet transform dictionary and the local discrete cosine transform dictionary to approximate the sparse components decomposed by MCA.

Curvelet transform (CT) dictionary: CT dictionary, Firstly, divide the frequency domain into wedge-shaped regions, and then use the local Fourier basis with direction to transform them. CT dictionary can sparsely express the flat region of the image [28]—that is, the lowfrequency part of the image.

Local discrete cosine transform (LDCT) dictionary: LDCT dictionary is an orthogonal transformation, which has good periodicity and can sparse the local texture structure of the image [28] (i.e., the high frequency part_. In essence, DCT is essentially a special form of discrete Fourier transform (DFT), and the coefficient of DCT represents the frequency content, analogous to that derived by Fourier analysis. DCT can represent the texture part of the image sparsely, whereas LDCT can represent the texture parts with uneven distribution.

2.6. Architecture of Proposed Method

The framework of the brain MRI denoising algorithm proposed in this paper is illustrated in Figure 6. It can be divided into four parts: stabilize noise variance (Step 1), decompose the image into a textures part and smooth part (Step 2), locally process the noise (Step 3, and Step 4), and combine two denoised parts and construct the final denoised MRI. Each step is detailed as follows:

- Step 1: Use VST to convert the Rician distribution of noise in the MRI into a Gaussian distribution.
- Step 2: Sparse decomposition of image: sparsely decompose the image by MCA, so as to separate the high frequency part and low frequency part of the image, and use the CT dictionary and the LDCT dictionary as the sub-dictionaries to represent the smooth part and texture details.
- Step 3: Design of adaptive threshold function: use the adaptive threshold estimation method based on wavelet transform to set the threshold [39] separately for the low frequency area sparsely represented by CT dictionary, and the high frequency area

sparsely represented by LDCT dictionary. The threshold processing strategy we adopted is a hard threshold, and the processing is as follows:

$$\hat{\omega}_{i,j} = \begin{cases} \omega_{i,j} & , \ |\omega_{i,j}| < T_x \\ 0 & , \ |\omega_{i,j}| \geq T_x \end{cases}. \tag{17}$$

That is, only retain the coefficients with greater modulus than the threshold. In (17) $\omega_{i,j}$ is the wavelet coefficient of each subband, T_x is the adaptive threshold of corresponding subband, $\hat{\omega}_{i,j}$ is the coefficient after threshold processing. In this method

$$T = 3\delta\delta_x, \tag{18}$$

where δ and δ_x are the standard deviation of noise and the standard deviation of coefficient matrix under a certain subband, respectively.

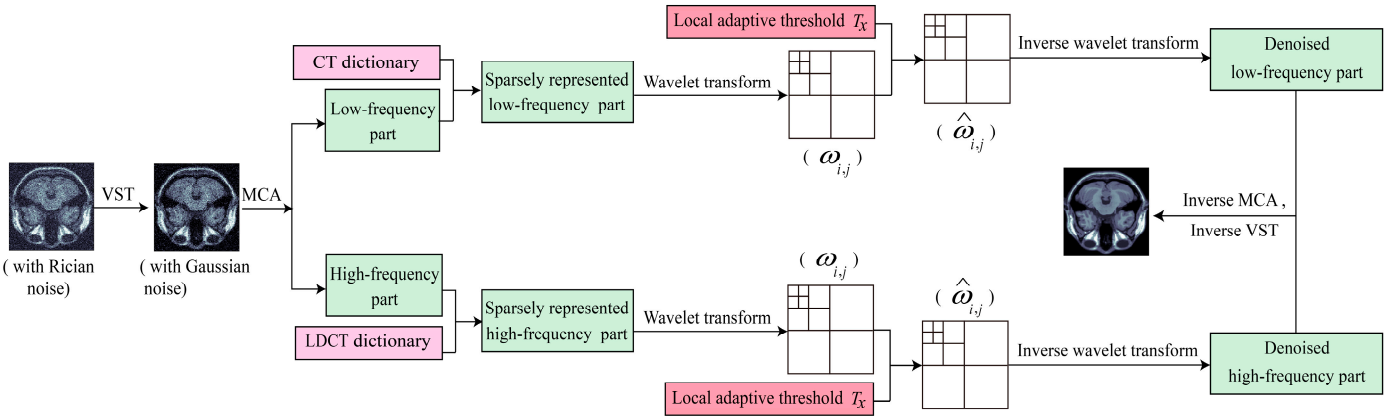

Figure 6. The overall structure of the proposed denoising method.

(1) Estimation of noise variance δ:

$$\delta_{(s,j)} = \frac{median\left|Y_{(s,j)}\right|}{0.6745}, \quad \left|Y_{(s,j)}\right| \in HH_j, \tag{19}$$

where $Y_{(s,j)}$ is the wavelet coefficients in the wavelet domain. $s = 1, 2, 3$ respectively represent horizontal coefficient HL_j, vertical coefficient LH_j and diagonal coefficient HH_j. $j = 1, 2, 3, \cdots N$ represents the number of decomposition layers, and N is the maximum decomposition layer.

(2) Estimation of the wavelet coefficient variance δ_x of the image:

After Step 1, image wavelet coefficients and noise wavelet coefficients are independent of each other, consequently

$$Y = X + Q, \tag{20}$$

$$\delta_Y^2 = \delta_X^2 + \delta^2, \tag{21}$$

where Y is the wavelet coefficient of the noisy image, X is the wavelet coefficient of the original image, Q is the wavelet coefficient of the noise. δ_Y^2 is variance of wavelet coefficients of noisy image, δ_X^2 is variance of wavelet coefficients of original image.

Since Y obeys Gaussian distribution, so

$$\delta_Y^2 = \frac{1}{n \times n} \sum_{i=1}^{n} \sum_{j=1}^{n} Y_{(i,j)}^2. \tag{22}$$

From (21) and (22), the standard deviation of the wavelet coefficients of the image X can be estimated as:

$$\hat{\delta}_X = \sqrt{\max(\hat{\delta}Y^2 - \hat{\delta}^2, 0)}. \tag{23}$$

- Step 4: Denoise each sparse layer of the image through different thresholds acquired from the adaptive threshold strategy inStep 3, separately.
- Step 5: Do inverse wavelet transform to obtain the denoised low frequency part and denoised high frequency part, and use inverse MCA to combine the two parts.
- Step 6: Construct the final denoised MRI by operating inverse VST.

2.7. Evaluation Criteria

Image evaluation methods can be divided into subjective classes and objective classes from the perspective of evaluation subjects. In the former, the human eye is the main body to evaluate the image quality; in the latter, the computer model is used to approximate the visual system of the human eye, and the quantitative index is designed to evaluate the image quality. The objective evaluation method is widely used in image quality evaluation of computer vision because it is not altered by the environment and humans. In objective image quality evaluation methods, the most extensively used criteria are peak signal-to-noise ratio (PSNR) [40], and structural similarity index (SSIM) [41].

(1) Peak Signal to Noise Ratio (PSNR)

PSNR reflects the fidelity of denoised image, and the higher the value, the better the fidelity. Its unit is decibels (dB). The smaller the value is, the more serious the distortion is. PSNR is defined as:

$$PSNR = 10\log_{10}\frac{M \times N[\max(f(i,j))]^2}{\sum_{i=1}^{M}\sum_{j=1}^{N}[h(i,j) - f(i,j)]^2}. \tag{24}$$

where $f(i,\ j)$ and $h(i,\ j)$ represent the pixel values of the reference image and the measured image at pixel position $(i,\ j)$, respectively, and $M \times N$ is the size of the image pixel matrix.

(2) Structural Similarity Index (SSIM)

SSIM contrasts the reference image and the estimated image in three dimensions, e.g., brightness, contrast and structure, and obtains value by weight multiplication. It reflects the similarity between the reference image and the tested image. $SSIM \in [-1, 1]$, and the larger the value, the higher the similarity. $SSIM$ is defined as:

$$SSIM = [L(f,h)]^{\alpha} \times [C(f,h)]^{\beta} \times [S(f,h)]^{\gamma}, \tag{25}$$

$$\begin{aligned} L(f,h) &= (2\mu_f\mu_h + C_1)/(\mu_f^2 + \mu_h^2 + C_1), \\ C(f,h) &= (2\sigma_f\sigma_h + C_2)/(\sigma_f^2 + \sigma_h^2 + C_2), \\ S(f,h) &= (\sigma_{fh} + C_3)/(\sigma_f\sigma_h + C_3), \end{aligned} \tag{26}$$

where f and h represent the reference image and the measured image; L, C, and S represent brightness similarity, contrast similarity and structure similarity, respectively; μ_f, and μ_h represent the average pixel value of f and h; σ_f, and σ_h represent the variance, and σ_{fh} represent covariance of the reference image and the measured image, respectively. α,β, and γ respectively represent the corresponding weight parameter, generally set to 1. C_1, C_2, and C_3 are three constants to avoid denominators being zero, generally, $C_1 = (k_1 \times L)^2$, $C_2 = (k_2 \times L)^2$, L is the specified dynamic range of the input image (255 for 8-bit grayscale), $k_1 \ll 1$, $k_2 \ll 1$. When $\alpha = \beta = \gamma = 1$ and $C_3 = C_2/2$, (25) can be simplified to:

$$SSIM = \frac{\left(2\mu_f\mu_h + C_1\right)\left(2\sigma_{fh} + C_2\right)}{\left(\mu_f^2 + \mu_h^2 + C_1\right)\left(\sigma_f^2 + \sigma_h^2 + C_2\right)}, \tag{27}$$

Although (27) is easy to calculate and has been processed in many previous studies, it is applicable to situations where brightness similarity, contrast similarity and structure

similarity have similar effects on image quality evaluation. The denoising algorithm designed in this article is aimed at medical MRI images, and contrast similarity and structural similarity play a relatively important role in evaluating the quality of medical images, compared with brightness similarity. Therefore, in this experiment, C and S are given relatively larger weights: $\alpha = \frac{1}{5}$, $\beta = \frac{2}{5}$, $\gamma = \frac{2}{5}$. So (25) can be simplified as:

$$SSIM = \left[\frac{\left(2\mu_f\mu_h + C_1\right)}{\left(\mu_f^2 + \mu_h^2 + C_1\right)}\right]^{\frac{1}{5}} \left[\frac{\left(2\sigma_{fh} + C_2\right)}{\left(\sigma_f^2 + \sigma_h^2 + C_2\right)}\right]^{\frac{2}{5}}, \tag{28}$$

In practical applications, the mean structural similarity ($MSSIM$) is used to estimate the structural similarity of the entire image, namely:

$$MSSIM = \frac{1}{J}\sum_{j=1}^{J} SSIM(x_j, y_j), \tag{29}$$

where, x_j and y_j represent the j-th partial image block in the original image and the denoised image, respectively, and J is the total number of partial windows. $MSSIM$ measures the structural similarity between the restored image and the original image. Among them, a larger $MSSIM$ value means that the restored image can better maintain the structural features of the original image.

2.8. Statistical Analysis

We calculated PSNR, and MSSIM values to evaluate the quality of denoised MRIs, and used the one-way analysis of variance (ANOVA) to compare the denoising effects of different approaches. $p < 0.01$ was considered statistically significant.

3. Results

All algorithms are encoded in matlab_R2020b_win64 environment. The same noised image datasets were used to ensure the validity and rationality of the evaluation results when comparing different denoising algorithms.

3.1. Denoising Results on Synthetic MRIs

The denoising results for different methods on the T1w, T2w, and PDw with different Rician noise levels are displayed in Tables 1–3 and Figure 7. The experimental data presented in Tables 1–3 are based on a sample size of 5430 synthetic brain MRIs. Each value in the table is the summed average value of PSNR and MSSIM of multiple images in the corresponding image group, providing an accurate representation of each group's performance. The average values in Tables 1–3 show that the proposed denoising method upgraded the PSNR, and MSSIM of noisy MRIs significantly, and improved them more significantly than bilateral filtering [42], anisotropic diffusion (AD) [43], nonlocal means filtering with non-subsampled shearlet transform (NST–NLM filtering) [44], Gaussian filtering [45], adaptive blockmatching and 3D (ABM3D) filtering [46], and nonlocal low-rank tensor approximation with logarithmic-sum regularization (NLRTA–LSR), filtering [47] for all noise levels (3%, 5%, 7%, 9%).

From Tables 1–3 and Figure 7, it can be seen that the SSIM value and PSNR value of the noise reduction results of each algorithm decrease with the increase of noise intensity in the image. From the six histograms in Figure 7a–f, it can be observed that AD have the largest variation amplitude of MSSIM and PSNR values with the change of noise in the three modalities of MRI datasets, whereas the variation amplitude of the proposed method in this paper is minimal.

Figure 7 also shows that the PSNR and MSSIM values between bilateral filtering, AD, and Gaussian filtering in each noise level data set (of T1w, T2w, and PDw) have little

difference, and are lower than those of the other four denoising algorithms; in contrast, the values of the proposed method in this paper are highest.

Table 1. Results for different compared methods on the T1w MRIs with different Rician noise levels.

Methods	3%		5%		7%		9%	
	PSNR (dB)	MSSIM	PSNR (dB)	MSSIM	PSNR (dB)	MSSIM	PSNR (dB)	MSSIM
Noisy images'	28.9690	0.7543	24.8977	0.6965	22.6711	0.6475	20.6069	0.5828
Bilateral filtering [42]	31.5046	0.8472	28.4792	0.7928	27.8130	0.7281	25.6071	0.6812
AD [43]	29.5920	0.8563	25.9117	0.7388	23.0982	0.6855	21.1842	0.6532
NST–NLM filtering [44]	37.2181	0.9631	34.6471	0.9428	32.4252	0.9371	31.6326	0.8972
Gaussian filtering [45]	30.0812	0.7932	26.7601	0.7371	25.7025	0.6931	22.7249	0.6280
ABM3D filtering [46]	36.2561	0.9581	34.0411	0.9355	31.9732	0.9176	29.0452	0.8526
NLRTA–LSR [47]	38.9526	0.9795	36.1028	0.9549	34.2501	0.9408	32.8904	0.9247
VST–MCAATE	40.2310	0.9862	39.4210	0.9830	38.7711	0.9820	37.8901	0.9738

Table 2. Results for different compared methods on the PDw MRIs with different Rician noise levels.

Methods	3%		5%		7%		9%	
	PSNR (dB)	MSSIM	PSNR (dB)	MSSIM	PSNR (dB)	MSSIM	PSNR (dB)	MSSIM
Noisy images'	27.3811	0.7592	23.4627	0.5319	21.2795	0.5018	20.6259	0.4075
Bilateral filtering [42]	30.6059	0.7906	27.4632	0.6801	27.3607	0.6428	25.0978	0.6096
AD [43]	29.7682	0.8573	25.8647	0.6036	23.1638	0.5307	21.8560	0.4769
NST–NLM filtering [44]	35.7480	0.9582	30.2139	0.9174	28.0752	0.8918	26.4628	0.8734
Gaussian filtering [45]	26.2501	0.7756	25.9355	0.6501	24.0371	0.6478	23.4001	0.5863
ABM3D filtering [46]	35.7634	0.9463	33.0832	0.9325	30.8031	0.8934	28.3591	0.8758
NLRTA–LSR [47]	39.1127	0.9704	37.4088	0.9631	36.3431	0.9459	33.4136	0.9206
VST–MCAATE	40.2260	0.9861	39.3893	0.9798	38.6811	0.9779	37.8560	0.9622

Table 3. Results for different compared methods on the T2w MRIs with different Rician noise levels.

Methods	3%		5%		7%		9%	
	PSNR (dB)	MSSIM	PSNR (dB)	MSSIM	PSNR (dB)	MSSIM	PSNR (dB)	MSSIM
Noisy images'	27.3551	0.7358	23.0532	0.6207	21.3520	0.5805	20.6149	0.4855
Bilateral filtering [42]	29.3853	0.7863	28.3904	0.7318	28.0345	0.7204	25.9146	0.6908
AD [43]	29.3790	0.8302	25.7041	0.7501	22.5302	0.6094	20.8501	0.4905
NST–NLM filtering [44]	35.5427	0.9363	31.2087	0.9227	29.1058	0.8943	27.5675	0.8901
Gaussian filtering [45]	28.0325	0.7812	26.1740	0.6738	24.6259	0.6031	23.6306	0.5703
ABM3D filtering [46]	34.2550	0.9492	31.3185	0.9204	29.0350	0.9154	28.5041	0.8926
NLRTA–LSR [47]	37.8633	0.9804	34.7425	0.9572	32.5816	0.9488	31.5804	0.9437
VST–MCAATE	40.0342	0.9859	39.4430	0.9829	38.7560	0.9792	36.8791	0.9803

The average PSNR and MSSIM values of different denoising methods in three modality datasets are displayed in Table 4, and their variation trend are displayed in Figure 8. It can be seen that the line of the PSNR and MSSIM values of ours are almost horizontal. The larger standard error values indicate that the denoising effect is influenced by different data modalities to a greater extent. The standard error values of PSNR and MSSIM of the proposed method are the lowest among the compared seven denoising methods.

Table 4. Average PSNR and MSSIM values of different methods in different modality datasets.

Methods	T1w		PDw		T2w		Mean ± SD/SE *	
	PSNR (dB)	MSSIM	PSNR (dB)	MSSIM	PSNR (dB)	MSSIM	PSNR (dB)	MSSIM
Noisy images'	24.2862	0.6703	23.1873	0.5501	23.0938	0.6056	23.5224 ± 0.5414/0.6631	0.6087 ± 0.0491/0.0602
Bilateral filtering [42]	28.3510	0.7623	27.6319	0.6808	27.9312	0.7323	27.9714 ± 0.2949/0.3612	0.7251 ± 0.0337/0.0412
AD [43]	24.9465	0.7335	25.1632	0.6171	24.6159	0.6701	24.9085 ± 0.2250/0.2756	0.6735 ± 0.0476/0.0583
NST-NLM filtering [44]	33.9808	0.9351	30.1250	0.9102	30.8562	0.9109	31.6540 ± 1.6722/2.0480	0.9187 ± 0.0116/0.0142
Gaussian filtering [45]	26.3172	0.7129	24.9057	0.6650	25.6158	0.6571	25.6129 ± 0.5762/0.7058	0.6783 ± 0.0247/0.0302
ABM3D filtering [46]	32.8289	0.9160	32.0022	0.9120	30.7782	0.9194	31.8698 ± 0.8424/1.0317	0.9158 ± 0.0030/0.0037
NLRTA-LSR [47]	35.5490	0.9500	36.5696	0.9500	34.1920	0.9575	35.4368 ± 0.9739/1.1928	0.9525 ± 0.0035/0.0043
VST-MCAATE	39.0783	0.9813	39.0381	0.9765	38.7781	0.9821	38.9648 ± 0.1331/0.1630	0.9799 ± 0.0025/0.0030

* SD: standard deviation; SE: standard error.

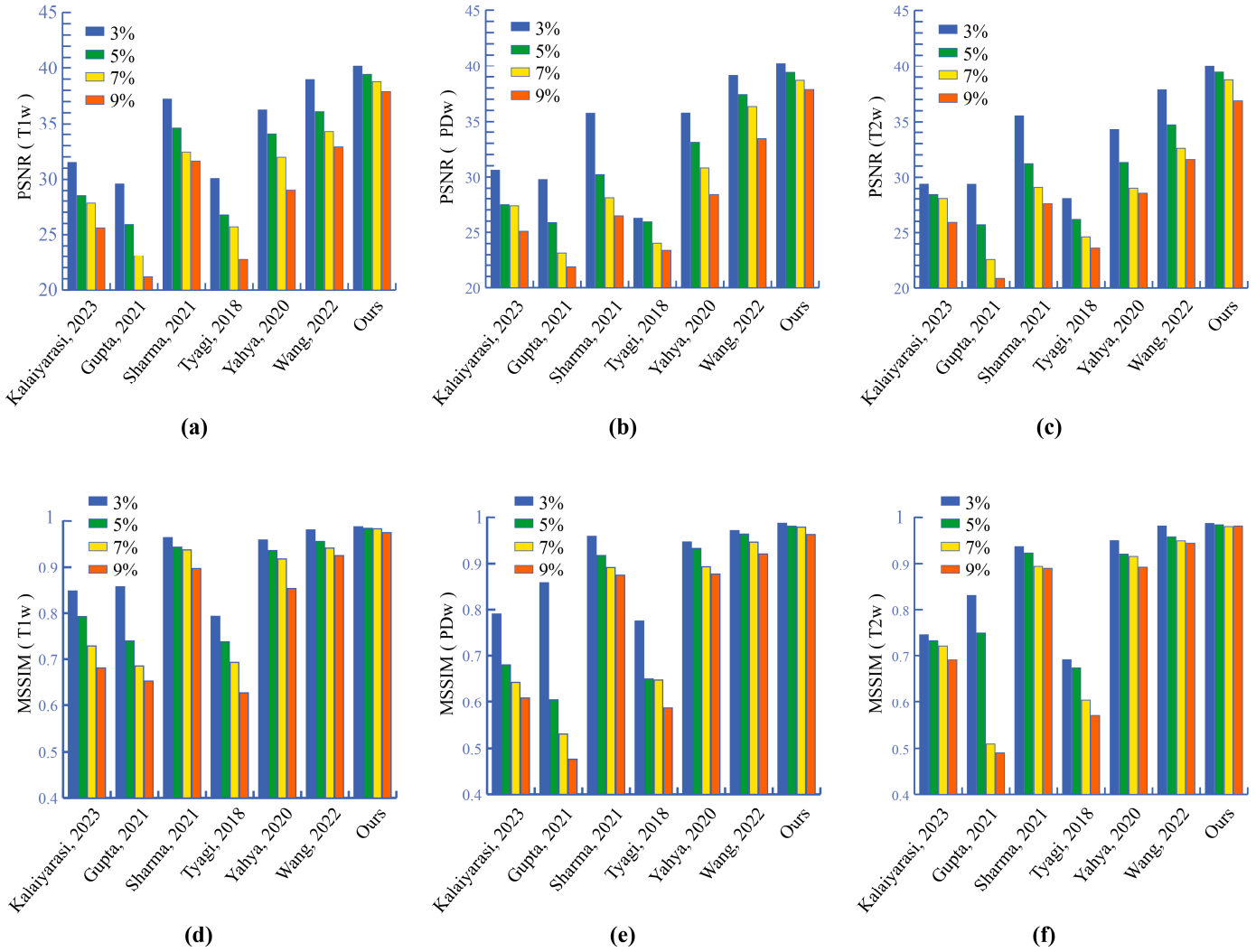

Figure 7. Comparison of PSNR/MSSIM values for different methods on the T1w/PDw/T2w MRI with different Rician noise levels. (**a**–**c**) are PSNR value histogram of different methods in T1w, PDw, T2w MRIs, separately; (**d**–**f**) are MSSIM value histogram of different methods in T1w, PDw, T2w MRIs, separately. Kalaiyarasi, 2023, used Bilateral filtering [42]; Gupta, 2021, used AD [43]; Sharma, 2021, used NST–NLM filtering [44]; Tyagi, 2018, used Gaussian filtering [45]; Yahya, 2020, used ABM3D filtering [46]; Wang, 2022, used NLRTA–LSR [47].

3.2. Evaluation of Real Clinical MRIs

The experimental results of the proposed method show clear advantages over the previous state-of-the-art algorithms. To use absolute clean MRIs as numerical references, we used the SBD, which is synthetic data, and may not be realistic enough. To prove the effectiveness of the proposed algorithm in removing noise in real clinical MRIs and avoid the contingency of denoising results at the same time, we also conducted further experiments using real clinical MR brain datasets [6,30]. A large number of experiments based on real clinical datasets showed that denoised MRIs are clearer than original real images, and residual images have no anatomical structure. Figure 9 is one of the experimental results with three modalities. Table 5 shows the average denoising results obtained from real brain datasets (113 2D-T1w, 184 2D-T2w, 136 2D-PDw, 581 3D-T1w, 578 3D-T2w, 578 3D-PDw).

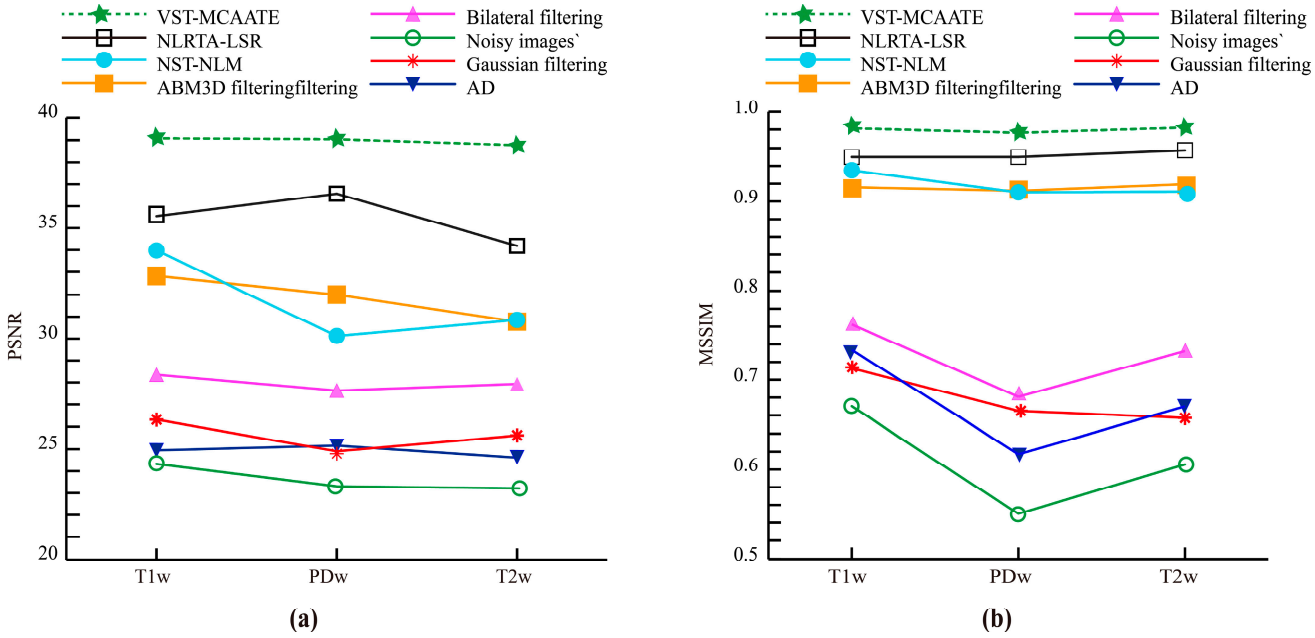

Figure 8. (**a**) Change trend of average PSNR value of different methods in different modality datasets. (**b**) Change trend of average MSSIM value of different methods in different modality datasets.

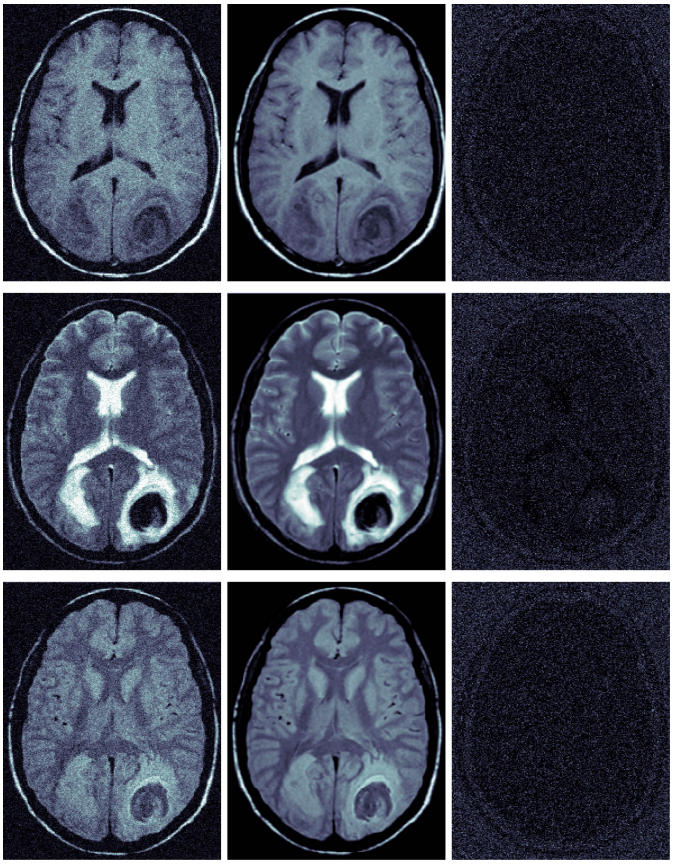

Figure 9. Real clinical images denoising examples (the 13th slice of brain tumor MRI was taken from a 22-year-old male brain tumor patient in the real clinical data set of Harvard University). From top to bottom, the left column represents real T1w, real T2w, and the real PDw; the middle column is the corresponding filtered images; the right column is the corresponding residual images (removed Rician noise).

Table 5. Average PSNR and MSSIM values of different methods (under single noise levels 3%, 5%, 7%, 9%, and mixed noise levels 3 + 5%, 3 + 5 + 7%).

Methods	PSNR (dB)	MSSIM
Bilateral filtering [42]	27.2930	0.7196
AD [43]	24.6760	0.6456
NST-NLM filtering [44]	31.5442	0.9021
Gaussian filtering [45]	25.5867	0.6612
ABM3D filtering [46]	31.4061	0.8913
NLRTA-LSR [47]	35.1065	0.9486
VST-MCAATE	38.7532	0.9781

3.3. Evaluation Focused on Diagnostic Tasks

The objective evaluation metrics (PSNR, MSSIM) used in this paper to assess denoising performance are based on the characteristics of the human visual system. These metrics are also highly sensitive to subtle variations in pixel values that are imperceptible to the human eye, and are therefore widely utilized for quantitative assessment of image quality in the field of image processing. However, evaluating the quality of medical images is different from natural images, as it not only requires consideration of the tampered pixel values and size, but also requires specific consideration of diagnostic tasks. Therefore, in this section, we ranked the opinion scores given by radiologists on denoised MRIs to subjectively compare the denoising effects of different algorithms.

To facilitate scoring and statistical analysis of the scoring results, we customized a MATLAB image window. Figure 10 shows the radiologists' scoring GUI interface designed in this paper. In the scoring interface, denoised images are randomly displayed to eliminate the influence of image display order on the scoring results. In the scoring interface, denoised MRIs are randomly displayed to eliminate the influence of image display order on the scoring results. The evaluation of denoised brain MRI quality is conducted from the perspective of professional radiologists, focusing on diagnostic tasks. The scoring is based on the confidence rating of the information extracted from the images. OLED screens use organic light-emitting diodes to emit light, with each pixel capable of independent illumination, ensuring consistent display effects from different viewing angles. Taking into account the varying heights and computer screen viewing habits of different experts, we used OLED screens to display the MRIs. We invited 13 radiologists to score each randomly displayed denoised image on a scale of 0–10, with higher scores indicating better image quality. We discarded abnormal values from the manual scoring results using the outlier removal method to ensure the reliability of the data. The remaining subjective scores were averaged to obtain the mean opinion score (MOS).

The comprehensive ranking results of different denoising algorithms (in terms of objective evaluation of denoising effects on three modality brain MRIs under four noise levels) are shown in Table 6. In addition, we have added the ranking results of two no-reference image quality evaluations in the table. The modified blind/referenceless image spatial quality evaluator (M-BRISQUE) [48] is an improvement on BRISQUE [49]. BRISQUE was originally designed for natural images and is one of the best state-of-the-art models in no-reference image quality evaluation, because it considers the luminance, image features and natural scene statistics of the image with very low computational complexity. In previous studies, it has been applied to the no-reference quality evaluation of ultrasound images [50] and MRI images [51]. Subsequent research [48] improved it and proposed a modified BRISQUE image quality evaluation method that is more suitable for MRIs. The improved method significantly increases sensitivity to Rician noise, and this paper therefore adopted M-BRISQUE. The objective measure of quality of denoised images (OMQDI) [52] also achieved a relatively high Pearson's linear correlation coefficient (PLCC) [53] in MRIs, making it a good choice for no-reference image quality evaluations. Figure 11a presents the histograms of MOS values of different algorithms in the comparative experiment, with the numbers in the circles indicating the final ranking results; Figure 11b is the

average histogram of the objective rankings of each denoising algorithm for all image sets, with the numbers in the circles indicating the final ranking results. As can be seen in Figure 11, NST–NLM filtering [44] and ABM3D filtering [46] have no significant difference in MRIs denoising effects; AD [43] and Gaussian filtering [45] also shows no significant difference. VST–MCAATE ranks at the top, showing significant differences when compared to other methods.

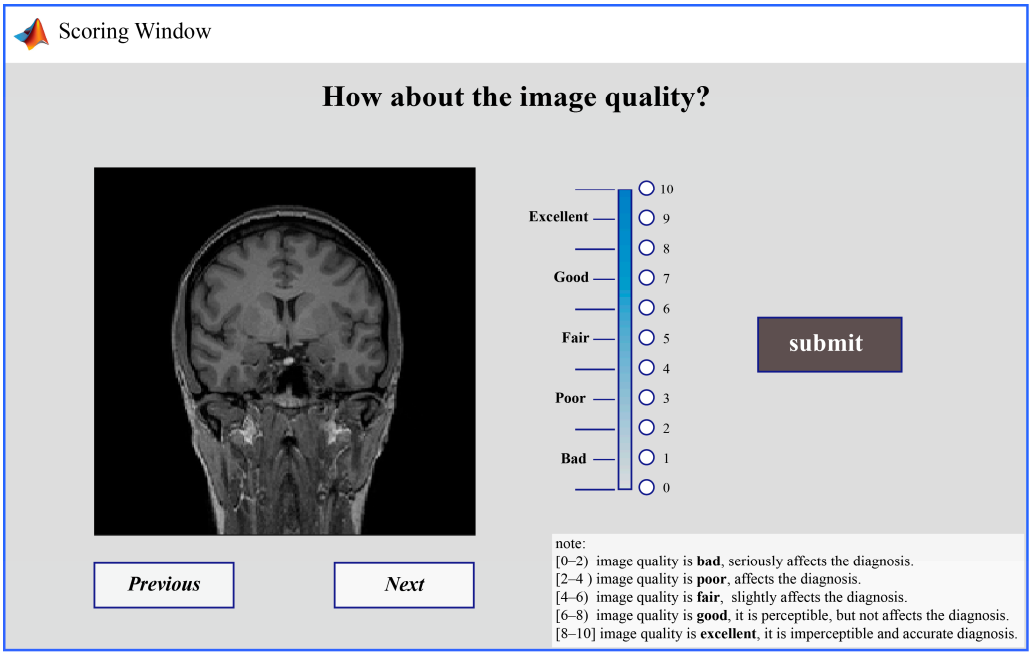

Figure 10. GUI interface used for image quality evaluation.

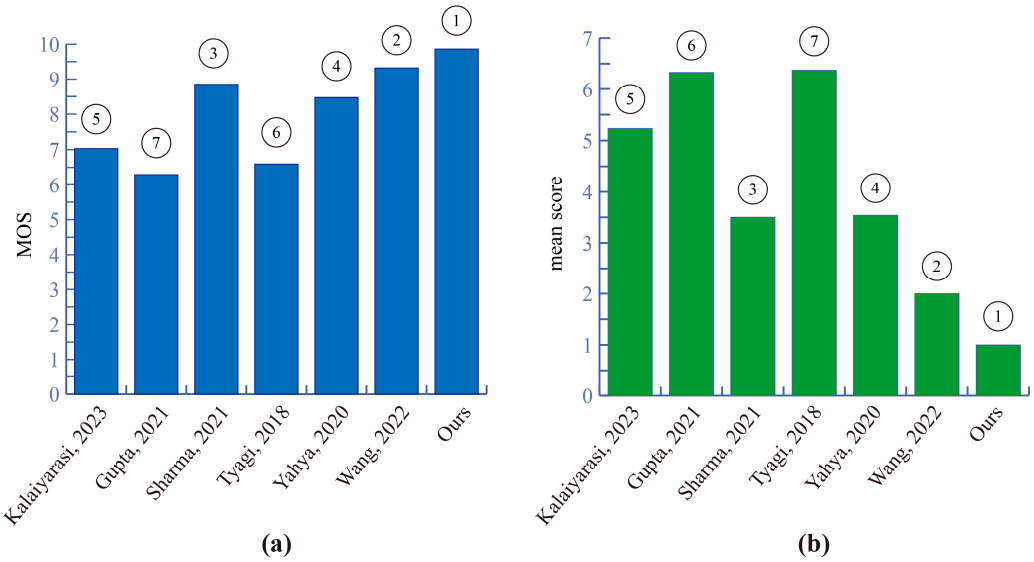

Figure 11. Matching of image quality for qualitative and quantitative evaluations: (**a**) Histograms of MOS values for each algorithm, (**b**) Histograms of average ranking of objective evaluation results for each algorithm. Kalaiyarasi, 2023, used Bilateral filtering [42]; Gupta, 2021, used AD [43]; Sharma, 2021, used NST–NLM filtering [44]; Tyagi, 2018, used Gaussian filtering [45]; Yahya, 2020, used ABM3D filtering [46]; Wang, 2022, used NLRTA–LSR [47]. The numbers in the circles are indicating the final ranking results.

Table 6. Rank score of different methods based on PSNR and MSSIM value.

Methods	PSNR																MSSIM									OMQDI	M-BRISQUE	T *	Mean Score	R
	T1w				PDw				T2w				T1w				PDw				T2w					Mixed	Mixed			
Bilateral filtering [42]	5	5	5	5	5	5	5	5	5	5	5	5	6	5	5	5	6	5	6	5	6	6	6	5	6	6	137	5.2692 ± 0.4436	5
AD [43]	7	7	7	7	6	7	7	7	6	7	7	7	5	6	7	6	5	7	7	7	5	5	5	7	3	5	163	6.2692 ± 1.0212	6
NST-NLM filtering [44]	3	3	3	3	4	4	4	4	3	4	3	4	3	3	3	3	3	4	4	4	4	3	4	4	4	3	91	3.5 ± 0.5	3
Gaussian filtering [45]	6	6	6	6	7	6	6	6	7	6	6	6	7	7	6	7	7	6	5	6	7	7	7	6	7	7	166	6.3846 ± 0.56	7
ABM3D filtering [46]	4	4	4	4	3	3	3	3	4	3	4	3	4	4	4	4	4	3	3	3	3	4	3	3	5	4	93	3.5769 ± 0.5666	4
NLRTA-LSR [47]	2	2	2	2	2	2	2	2	2	2	2	2	2	2	2	2	2	2	2	2	2	2	2	2	2	2	52	2 ± 0	2
VST-MCAATE	1	1	1	1	1	1	1	1	1	1	1	1	1	1	1	1	1	1	1	1	1	1	1	1	1	1	24	1 ± 0	1

* T: total score; R: final rank.

4. Discussion

In this paper, we proposed a dedicated noise reduction method to MRIs to upgrade the reliability and accuracy of brain MRI application and analysis, which was named VST–MCAATE, and tested on three independent datasets. This method has two most important advantages: First, the sparse representation and multi decomposition designed in this study enable the denoising model to solve the problem of useful information and noise overlapping in the frequency band, which can in turn preserve complex texture details of MRIs while denoising; second, the variance of the noisy pixel, and the variance of the non-noisy pixel were both taken into consideration while setting the threshold model, and the threshold is locally adaptive, which both mean the model has a better ability to identify noisy and non-noisy pixels. Consequently, the proposed method can also have a good denoising effect when the noise distributions and intensity are unknown, and can remove the noise as much as possible without misclassifying the non-noisy pixel. Experimental results show that denoising method proposed in our study outperforms state-of-the-art methods (bilateral filtering, AD, NST–NLM filtering, Gaussian filtering, ABM3D filtering, and NLRTA–LSR), in terms of obtaining better PSNR values and MSSIM values, and demonstrating strong stable noise reduction capability in different modes and at different noise levels.

In compared experiments, the numerical results of PSNR and MSSIM decrease with the increase of noise intensity, which indicates that the degree of noise pollution directly affects the denoising effect of each denoising model, and also that the denoising effect will decrease with the increase of noise pollution degree. In real clinical MRIs, the noise level is unknown, and various levels of noise may exist, which establishes that denoising robustness at different noise levels is as important as the denoising effect at a certain noise level. Therefore, we also compared the noise robustness of each denoising model. The variation amplitude of the MSSIM value and PSNR value of methods at different noise levels indicates that the noise robustness of the proposed method is the best among them.

Comparison results of PSNR and SSIM values of each denoising model at different noise levels indicate that the denoising effect of bilateral filtering, AD, and Gaussian filtering is ordinary, while the denoising effect of the proposed method in this paper is the most outstanding, when considered against the latest and most advanced (six) noise reduction algorithms that operate in various noise intensities. The variation trend and standard deviation of SSIM and PSNR values for different methods in different modality datasets indicate that the denoising effects of the proposed method are almost the same in each modality (T1w, T2w, PDw) of MRI datasets; However, other compared methods are more or less influenced by the modality of MRI data. The denoising results of real clinical MRIs indicate that VST–MCAATE can effectively remove the Rician noise of the brain MRIs without affecting the original anatomical structure of the image. The evaluation results focused on diagnostic tasks indicate that the comprehensive subjective evaluation ranking results and objective evaluation ranking results of the (seven) compared algorithms remain consistent; when the focus is on diagnostic tasks, the denoising algorithm proposed in this paper still performs the best.

Although this method has many advantages, it also has several limitations. First, due to the limitations of the reference MRIs on the global database (GDB), the denoising experiments used conventional sequences MR datasets, and did not verify the effect on MR datasets with different scanning modes, such as diffusion tensor imaging (DTI). Second, the edge detection method or the multi-modal fusion method can be added to the proposed denoising process to obtain high-quality clinical images with enhanced edges and textures. But its denoising effect cannot be evaluated and compared with the state-of-the-art methods quantitatively by objective evaluation criteria because there are no standard fused noise-free reference image datasets. If the subjective evaluation method is to be used to evaluate the effect of image quality improvement, then many professional doctors need to evaluate it by eye observation scoring. Then, quantitative comparisons can be made. We are committed to continuously refining and enriching our research to solve the potential limitations.

5. Conclusions

This paper proposed a dedicated noise reduction method for brain MRIs. A large number of experiments have used SBD and real clinical data to show that the proposed denoising method has advantages in upgrading the quality of medical MRIs, which is due to it protecting the edge contour and texture details while effectively removing the noise with different and unknown noise levels. This method also has strong noise robustness, and its denoising effects are not limited by different MRI modalities. The proposed method significantly outperforms state-of-the-art methods, such as bilateral filtering, Gaussian filtering, AD, NST–NLM filtering, NLRTA–LSR filtering, and ABM3D filtering, in achieving higher PSNR and MSSIM. This method can, in reconstructing high-quality MRIs with a clearer and more precise anatomical structure of human soft tissue, upgrade the reliability and accuracy of brain MRI application and analysis. In this and other respects, the method continues to demonstrate potential clinical promises.

Author Contributions: Conceptualization, B.A., P.Y. and J.Y.; methodology, B.A., P.Y. and J.Y.; software, B.A. and P.Y.; validation, B.A., P.Y. and J.Y.; formal analysis, B.A. and J.Y.; investigation, B.A.; resources, Q.L.; writing—original draft preparation, B.A. and P.Y.; writing—review and editing, B.A. and Q.L.; supervision, Q.L.; project administration, Q.L.; funding acquisition, Q.L. and J.Y. All authors have read and agreed to the published version of the manuscript.

Funding: This research was funded by the National Natural Science Foundation of China [grant number: 61672335]; the Colleges Innovation Project of Guangdong, China [grant number: 2017KCXTD015]; the Guangdong Provincial University Innovation Team Project [grant number: 2020KCXTD012], and Jilin Provincial Scientific and Technological Development Program [grant number: 20200802004GH].

Data Availability Statement: The data presented in this study are publicly available data (sources are stated in the citations [6,29,30]).

Acknowledgments: The authors would like to thank all those who provided raw data; they would also like to thanks all editors and reviewers, and their radiology friends at Akesu First People's Hospital and Nongyishi Hospital for participating in the subjective evaluation experiment.

Conflicts of Interest: The authors declare no conflicts of interest. The funders had no role in the design of the study, the collection, analyses, or interpretation of data, the writing of the manuscript, or the decision to publish the results.

References

1. Theodorou, D.J.; Theodorou, S.J.; Petsanas, A.P. Whole-body MR imaging for improved detection of neurofibromatosis: An integrated technical note to estimate true extent. *Neurosurg. Rev.* **2023**, *46*, 236. [CrossRef]
2. Mishro, P.K.; Agrawal, S.; Panda, R.; Abraham, A. A survey on state-of-the-art denoising techniques for brain magnetic resonance images. *IEEE Rev. Biomed. Eng.* **2022**, *15*, 184–199. [CrossRef] [PubMed]
3. Yu, H.; Ding, M.; Zhang, X. Laplacian eigenmaps network-based nonlocal means method for MR image denoising. *Sensors* **2019**, *19*, 2918. [CrossRef] [PubMed]
4. Shukla, V.; Khandekar, P.; Khaparde, A. Noise estimation in 2D MRI using DWT coefficients and optimized neural network. *Biomed. Signal Process. Control* **2022**, *71*, 103225. [CrossRef]
5. Henkelman, R.M. Measurement of signal intensities in the presence of noise in MR images. *Med. Phys.* **1985**, *12*, 232–233. [CrossRef] [PubMed]
6. Hill, D.; Williams, S.; Hawkes, D.; Smith, S. IXI Dataset: IXI-Information Extraction from Images Project (EPSRC GR/S21533/02). 2021. Available online: https://brain-development.org/ixi-dataset (accessed on 1 January 2024).
7. Ilesanmi, A.E.; Ilesanmi, T.O. Methods for image denoising using convolutional neural network: A review. *Complex Intell. Syst.* **2021**, *7*, 2179–2198. [CrossRef]
8. Salamat, N.; Missen, M.M.S.; Prasath, V.B.S. Recent developments in computational color image denoising with PDEs to deep learning: A review. *Artif. Intell. Rev.* **2021**, *54*, 6245–6276. [CrossRef]
9. Kaur, A.; Dong, G.F. A complete review on image denoising techniques for medical images. *Neural. Process. Lett.* **2023**, *55*, 7807–7850. [CrossRef]
10. Singh, A.K. Major development under Gaussian filtering since unscented Kalman filter. *IEEE/CAA J. Autom. Sin.* **2020**, *7*, 1308–1325. [CrossRef]
11. Liu, R.; Li, Y.; Wang, H.; Liu, J. A noisy multi-objective optimization algorithm based on mean and Wiener filters. *Knowl.-Based Syst.* **2021**, *228*, 107215. [CrossRef]

12. Liang, W.; Long, J.; Li, K.C.; Xu, J.; Lei, X. A fast defogging image recognition algorithm based on Bilateral Hybrid filtering. *ACM Trans. Multimed. Comput. Commun. Appl.* **2021**, *17*, 42. [CrossRef]
13. Shi, B.L.; Li, M.X.; Luo, Y.F. Adaptively weighted difference model of anisotropic and isotropic total variation for image denoising. *J. Nonlinear Var. Anal.* **2023**, *7*, 563–580. [CrossRef]
14. Bhujle, H.V.; Vadavadagi, B.H. NLM based magnetic resonance image denoising—A review. *Biomed. Signal Process. Control* **2019**, *47*, 252–261. [CrossRef]
15. Elaiyaraja, G.; Kumaratharan, N.; Rao, T.C.S. Fast and efficient filter using wavelet threshold for removal of Gaussian noise from MRI/CT scanned medical images/color video sequence. *IETE J. Res.* **2022**, *68*, 10–22. [CrossRef]
16. Bal, A.; Banerjee, M.; Sharma, P.; Maitra, M. An efficient wavelet and Curvelet-based PET image denoising technique. *Med. Biol. Eng. Comput.* **2019**, *57*, 2567–2598. [CrossRef]
17. Hemalatha, J.; Devi1, M.K.K.; Geetha, S. Improving image steganalyser performance through curvelet transform denoising. *Clust. Comput.* **2019**, *22*, 11821–11839. [CrossRef]
18. Liu, P.; Basha, M.D.E.; Li, Y.J.Y.; Xiao, Y.; Sanelli, P.C.; Fang, R.G. Deep evolutionary networks with expedited genetic algorithms for medical image denoising. *Med. Image Anal.* **2019**, *54*, 306–315. [CrossRef]
19. Zhang, C.J.; Huang, X.Y.; Fang, M.C. MRI denoising by NeighShrink based on chi-square unbiased risk estimation. *Artif. Intell. Med.* **2019**, *97*, 131–142. [CrossRef]
20. Ji, L.L.; Guo, Q.; Zhang, M.L. Medical image denoising based on biquadratic polynomial with minimum error constraints and low-rank approximation. *IEEE Access* **2020**, *8*, 84950–84960. [CrossRef]
21. He, J.F.; Gao, P.; Zheng, X.N.; Zhou, Y.T.; He, H. Denoising 3D magnetic resonance images based on weighted tensor nuclear norm minimization using balanced nonlocal patch tensors. *Biomed. Signal Process. Control* **2022**, *74*, 103524. [CrossRef]
22. Tian, Q.Y.; Li, Z.Y.; Fan, Q.Y.; Polimeni, J.R.; Bilgic, B.; Salat, D.H.; Huang, S.Y. SDnDTI: Self-supervised deep learning-based denoising for diffusion tensor MRI. *Neuroimage* **2022**, *253*, 119033. [CrossRef]
23. Lin, T.T.; Wei, M.; Zhang, Y. Deep learning for denoising: An attempt to recover the effective magnetic resonance sounding signal in the presence of high level noise. *IEEE Trans. Geosci. Remote Sens.* **2022**, *60*, 5910613. [CrossRef]
24. Nowak, R.D. Wavelet-based Rician noise removal for magnetic resonance imaging. *IEEE Trans. Image Process.* **1999**, *8*, 1408–1419. [CrossRef]
25. Foi, A. Noise estimation and removal in MR imaging: The variance-stabilization approach. In Proceedings of the 2011 IEEE International Symposium on Biomedical Imaging: From Nano to Macro, Chicago, IL, USA, 30 March–2 April 2011; pp. 1809–1814. [CrossRef]
26. Yang, J.; Fan, J.F.; Ai, D.; Zhou, S.J.; Tang, S.Y.; Wang, Y.T. Brain MR image denoising for Rician noise using pre-smooth non-local means filter. *Biomed. Eng. Online* **2015**, *14*, 2. [CrossRef]
27. Khaleel, H.S.; Sagheer, S.V.M.; Baburaj, M.; George, S.N. Denoising of Rician corrupted 3D magnetic resonance images using tensor-SVD. *Biomed. Signal Process. Control* **2018**, *44*, 82–95. [CrossRef]
28. Fadili, J.M.; Starck, J.L.; Elad, M.; Donoho, D.L. MCALab: Reproducible research in signal and image decomposition and inpainting. *Comput. Sci. Eng.* **2010**, *12*, 44–62. [CrossRef]
29. BrainWeb: Simulated Brain Database. 2011. Available online: http://mouldy.bic.mni.mcgill.ca/brainweb/ (accessed on 1 January 2024).
30. Johnson, K.A.; Becker, J.A. The Whole Brain Atlas, 20 August 1997. Available online: http://www.med.harvard.edu/AANLIB (accessed on 1 January 2024).
31. Watson, G.N. Bessel Functions. In *A Treatise on the Theory of Bessel Functions*, 2nd ed.; Cambridge University Press: Cambridge, UK, 1945; Chapter 3; pp. 38–84. [CrossRef]
32. Routray, S.; Ray, A.K.; Mishra, C. Image denoising by preserving geometric components based on weighted Bilateral filter and Curvelet transform. *Optik* **2018**, *159*, 333–343. [CrossRef]
33. Saudagar, A.K.J.; Syed, A.S. Image compression approach with Ridgelet transformation using modified neuro modeling for biomedical images. *Neural Comput. Appl.* **2014**, *24*, 1725–1734. [CrossRef]
34. Yang, S.Y.; Min, W.; Zhao, L.F.; Wang, Z.Y. Image noise reduction via geometric multiscale Ridgelet support vector transform and dictionary learning. *IEEE Trans. Image Process.* **2013**, *22*, 4161–4169. [CrossRef] [PubMed]
35. Cloninger, A.; Li, H.T.; Saito, N. Natural graph wavelet packet dictionaries. *J. Fourier Anal. Appl.* **2021**, *27*, 41. [CrossRef]
36. Khmag, A.; Ramli, A.R.; Kamarudin, N. Clustering-based natural image denoising using dictionary learning approach in wavelet domain. *Soft Comput.* **2019**, *23*, 8013–8027. [CrossRef]
37. He, H.J.; Liang, J.Z.; Hou, Z.J.; Di, L.; Xia, Y.F. Multi-pose face reconstruction and Gabor-based dictionary learning for face recognition. *Appl. Intell.* **2023**, *53*, 16648–16662. [CrossRef]
38. Koley, S.; Roy, H.; Dhar, S.; Bhattacharjee, D. Cross-modal face recognition with illumination-invariant local discrete cosine transform binary pattern (LDCTBP). *Pattern Anal. Appl.* **2023**, *26*, 847–859. [CrossRef]
39. Si, W.; Qin, B.Y.; Li, Q.G.; Liu, H.X. A novel adaptive wavelet threshold estimation based on hybrid particle swarm optimization for partial discharge signal denoising. *Optik* **2019**, *181*, 175–184. [CrossRef]
40. Tanchenko, A. Visual-PSNR measure of image quality. *J. Vis. Commun. Image Represent.* **2014**, *25*, 874–878. [CrossRef]
41. Wang, Z.; Bovik, A.C.; Sheikh, H.R.; Simoncelli, E.P. Image quality assessment: From error visibility to structural similarity. *IEEE Trans. Image Process.* **2004**, *13*, 600–612. [CrossRef] [PubMed]

42. Kalaiyarasi, M.; Janaki, R.; Sampath, A.; Ganage, D.; Chincholkar, Y.D.; Budaraju, S. Non-additive noise reduction in medical images using bilateral filtering and modular neural networks. *Soft Comput.* 2023, *early access*. [CrossRef]
43. Gupta, B.; Lamba, S.S. An efficient anisotropic diffusion model for image denoising with edge preservation. *Comput. Math. Appl.* **2021**, *93*, 106–119. [CrossRef]
44. Sharma, A.; Chaurasia, V. MRI denoising using advanced NLM filtering with non-subsampled Shearlet transform. *Signal Image Video Process.* **2021**, *15*, 1331–1339. [CrossRef]
45. Tyagi, V. Image Denoising. In *Understanding Digital Image Processing*, 1st ed.; CRC Press: London, UK; New York, NY, USA, 2018; Chapter 6; pp. 76–84. [CrossRef]
46. Yahya, A.A.; Tan, J.Q.; Su, B.Y.; Hu, M.; Wang, Y.B.; Liu, K.; Hadi, A.N. BM3D image denoising algorithm based on an adaptive filtering. *Multimed. Tools Appl.* **2020**, *79*, 20391–20427. [CrossRef]
47. Wang, L.; Xiao, D.; Hou, W.S.; Wu, X.Y.; Jiang, B.; Chen, L. A nonlocal enhanced Low-Rank tensor approximation framework for 3D magnetic resonance image denoising. *Biomed. Signal Process. Control* **2022**, *72*, 103302. [CrossRef]
48. Chow, L.S.; Rajagopal, H. Modified-BRISQUE as no reference image quality assessment for structural MR images. *Magn. Reson. Imag.* **2017**, *43*, 74–87. [CrossRef] [PubMed]
49. Mittal, A.; Moorthy, A.K.; Bovik, A.C. No-reference image quality assessment in the spatial domain. *IEEE Trans. Image Process.* **2012**, *21*, 4695–4708. [CrossRef]
50. Ardakani, A.A.; Mohammadi, A.; Faeghi, F.; Acharya, U.R. Performance evaluation of 67 denoising filters in ultrasound images: A systematic comparison analysis. *Int. J. Imaging Syst. Technol.* **2023**, *33*, 445–464. [CrossRef]
51. Lim, A.; Lo, J.; Wagner, M.W.; Ertl-Wagner, B.; Sussman, D. Motion artifact correction in fetal MRI based on a Generative Adversarial network method. *Biomed. Signal Process. Control* **2022**, *81*, 104484. [CrossRef]
52. Simi, V.R.; Edla, D.R.; Joseph, J. A no-reference metric to assess quality of denoising for Magnetic Resonance images. *Biomed. Signal Process. Control* **2021**, *70*, 102962. [CrossRef]
53. Wiedermann, W.; Hagmann, M. Asymmetric properties of the Pearson correlation coefficient: Correlation as the negative association between linear regression residuals. *Commun. Stat.-Theory Methods* **2016**, *45*, 6263–6283. [CrossRef]

Disclaimer/Publisher's Note: The statements, opinions and data contained in all publications are solely those of the individual author(s) and contributor(s) and not of MDPI and/or the editor(s). MDPI and/or the editor(s) disclaim responsibility for any injury to people or property resulting from any ideas, methods, instructions or products referred to in the content.